Influence of sodium 5-sulfosalicylate as a corrosion inhibitor in NaCl electrolyte on enhanced performances of Mg-air batteries

Yaqing Zhou, Sandrine Zanna, Antoine Seyeux, Luntao Wang, Philippe Marcus, Jolanta Światowska

Influence of sodium 5-sulfosalicylate as a corrosion inhibitor in NaCl electrolyte on enhanced performances of Mg-air batteries

Yaqing Zhou, Sandrine Zanna, Antoine Seyeux, Luntao Wang, Philippe Marcus,

Jolanta Światowska

Chimie ParisTech - CNRS, PSL University, Institut de Recherche de Chimie Paris,

11 rue Pierre et Marie Curie, Paris 75005, France

Abstract

This work aims at employing sodium 5-sulfosalicylate (5-S-Sal) corrosion inhibitor into aqueous NaCl electrolyte to improve the discharge performance of Mg-air battery and decrease the side reactions of Mg anode. The corrosion tests at open circuit potential show a four-fold decrease of hydrogen evolution when 5-S-Sal inhibitor is added. X-ray photoelectron spectroscopy and time-of-flight secondary ion mass spectrometry analyses show that due to the presence of 5-S-Sal inhibitor, a corrosion resistant layer has a lower quantity of $Mg(OH)_2$ (by ~15%) than that formed in NaCl electrolyte. The surface enrichment in S-like species originating from inhibitor molecule could have an important effect on a decreased corrosion and slow down the H_2 evolution. Within a range of concentrations of 5-S-Sal in NaCl electrolyte (0.05 M to 0.15 M), the best discharge performances are achieved with 0.1 M inhibitor. The discharge voltage of full Mg-air battery improves from ~1.58 V to ~1.82 V at 0.5 mA/cm^2 and the discharge lifetime is extended from around 12.5 to around 80 hours. Scanning electron microscopy and 3D topography laser microscopy indicate that during the discharge tests much smaller surface degradation occurs and a more uniform surface layer is formed in the presence of inhibitor in the NaCl-based electrolyte.

1. Introduction

Lithium-ion batteries [1-5] are widely used and commercially available energy storage technologies, however their energy density of 150-250 Wh/kg and safety are limited for extended use for large grid-scale stationary applications [6]. It is generally known that the further improvements on Li-ion batteries can lead to 30% increase in their energy density [7], therefore, the high-energy-density energy storage systems are extremely desired. Primary magnesium air batteries that applied NaCl aqueous based electrolyte have been an intensive research subject due to their low cost and high safety [8-10]. Considering the chemistries of actually widely used Li-ion batteries (using cobalt, nickel for cathode manufacturing or toxic electrolytes and binders), the Mg-air batteries are also more environmentally, socially responsible and they stand out as clean energy technologies [11]. As one kind of multivalent metal-oxygen/air batteries, Mg-air batteries exhibit high theoretical voltage of 3.1 V, high specific capacity of 2.22 Ah/g and high specific energy density of 6.8 kWh/kg [12, 13]. Mg-air batteries with an open cell construction consume oxygen from air and Mg metal as anode, which can be replaced by new Mg plate when the Mg metal is exhausted [14].

However, Mg is very active as a metal and suffers seriously from self-corrosion (related to the micro-galvanic coupling between Mg matrix and metallic impurities such as Fe [15, 16]) and chunk effect, which is caused by the detachment of metallic particles [15]. Due to Mg corrosion, the discharge products such as MgO, $Mg(OH)_2$ and $MgCO_3$ accumulate on the Mg surface [17, 18] can block the Mg anode surface. For these reasons, the coulombic efficiency can be significantly decreased and thus the practical

specific energy of full Mg-air batteries is reduced [8]. As a result, the working voltage and actual discharge performance of Mg-air batteries are greatly lower than their theoretical values. To overcome these problems, numerous works were focused on searching new types of Mg alloys. Various metals, such as Al, La, Gd, Zn Li, *etc.* [19-21] alloyed with Mg lead to a decrease of the side reactions of Mg anode and improve the utilization efficiency. Nowadays, more and more studies are focused on the electrolyte. Wang's group [22] applied organic/inorganic mixed solution as electrolyte for Mg-air batteries. Höche *et al.* employed Fe^{3+} complexing agent, like salicylate, to boost battery performance [23]. Adding tailoring additives into electrolyte, such as citric acid, salicylic acid, is also an interesting way to enhance the discharge behavior of full Mg-air batteries [24]. However, the acid will also damage the oxide surface film of Mg anode. There have been few studies conducted on influence of aqueous electrolytes and their additives on the reactivity of Mg anode in Mg-air batteries. The interfacial properties of Mg anode/electrolyte should be tailored in order to improve the performance of Mg-air batteries. Therefore, in this work we propose to apply one of the most interesting corrosion inhibitors: the sodium 5-sulfosalicylate (5-S-Sal) in 0.6 M NaCl electrolyte for Mg-air batteries. The pure commercial Mg anode (99.9%) as a model electrode material was used instead of Mg alloy in order to discard the interference with the alloying elements in the alloy and better understand the influence of 5-S-Sal inhibitor added to electrolyte and its working mechanism. Different immersion times of Mg anode in electrolyte with and without inhibitors were applied to elucidate the progress of Mg corrosion and analyze the corrosion of Mg by linear

sweep voltammetry and electrochemical impedance spectroscopy. The surface chemical composition of Mg anode was analyzed by X-ray Photoelectron Spectroscopy (XPS) and Time-of-Flight Secondary Ion Mass Spectrometry (ToF-SIMS). According to our knowledge this is for the first time that the surface of the Mg electrode is studied combining these two analytical methods, which allows for a fine surface and in-depth characterization of the surface layer. Then, after the corrosion studies, different concentrations of 5-S-Sal were used to compare the discharge behaviors with the objective to tune the best battery performance *i.e.*, the highest discharge voltage and the longest battery lifetime. The composition and morphology of the Mg anode was also analyzed after discharge tests to demonstrate its improved performance in electrolyte in the presence of inhibitor.

2. Materials and methods

2.1 Samples and electrolyte preparation

Mg plate (≥99.9 wt%) purchased from a chemical company was cut into small pieces of 15*15*1 mm^3 in size. The composition of the pure Mg is given in Table S1. SiC abrasive paper (#400, #2400, #4000) was used to ground Mg samples prior to the electrochemical measurements and diamond grinding paste (3, 1 and 0.25 μm) was employed to polish the samples for the surface characterization by X-ray photoelectron spectroscopy (XPS) and time-of-flight secondary ions mass spectrometry (ToF-SIMS). Between each step, samples were rinsed with pure water and finally dried by filtered compressed air. 0.6 M NaCl (AnalaR Normapur, analysis reagent, VMR) in ultra-pure H_2O (Millipore, resistivity > 18.5 MΩ.cm) with or without sodium 5-sulfosalicylate (5-

S-Sal) (Sinopharm Chemical Reagent Co. Ltd) acid was used as electrolyte.

2.2 Electrochemical measurement and H_2 evolution test

Open circuit potential (OCP), linear sweep voltammetry (LSV) and electrochemical impedance spectroscopy (EIS) were performed using the EC-Lab SP200 potentiostat (BioLogic Science Instruments SAS). A classical 3-electrode electrochemical cell was used with an Ag/AgCl reference electrode, a platinum foil as a counter electrode and Mg samples as working electrodes. The tested area of Mg sample of 1.1 cm^2 was delimited by a viton o-ring. The volume of hydrogen evolution was measured using an inverted burette with a funnel installed above the Mg sample placed at the bottom of the cell [25]. The volume of hydrogen evolution was recorded every 10 min at OCP during 500 min of immersion. Each experiment was repeated at least three times and the mean and standard deviation values were calculated. Polarization curves were performed at a scan rate of 1 mV/s from E_{OCP} -0.5 V to E_{OCP} +0.5 after various immersion times (15, 30, 60, 300 and 400 min). EIS measurements were carried out with a frequency from 100 kHz to 0.1 Hz after 15, 60, 300 and 400 min of immersion at OCP. The spectra were fitted with equivalent circuits using ZSimpWin 3.3d software.

2.3 Microstructure characterization (SEM, Optical Microscope）

A digital VHX-500 Keyence microscope was employed to analyze Mg anode surface morphologies after immersion in electrolyte with and without inhibitor. Scanning electron microscopy (SEM, Zeiss Ultra 55) was used for further analysis of Mg samples after immersion tests at OCP and cross-section morphologies after discharge tests.

2.4 Battery discharge tests

A home-made electrochemical cell made of PVDF plastic was used to test the discharge performance of full Mg-air battery. It was composed of two electrodes of Mg anode, and commercial air cathode mounted parallelly to each other and separated by a distance of 5 mm and 0.6 M NaCl solution with or without inhibitor as an electrolyte. The volume of electrolyte was 17.5 ml. The air can diffuse freely through the back side of the porous and air permeable cathode. For a reliable comparison of the discharge performance of Mg electrodes, similar Mg plates (15*15*1 mm^3) were used in all tests. The air cathode was Pt/C (20 wt% of Pt, bought from Alfa Aesar, France) dripped on the surface of commercial air cathode (bought from Yoteco company, China), with the catalyst (Pt/C) loading of 1 mg/cm^2. The working areas of the cathode and anode are both 1.1 cm^2 which delimited by a Viton O-ring. LAND BT 2000 battery test system was used to measure the discharge performances of full Mg-air battery at different current densities.

2.5 Surface analysis (ToF-SIMS and XPS)

ToF-SIMS and XPS were combined to analyze the surface chemical composition of Mg anode. A ToF-SIMS V spectrometer (ION TOF-Münster, Germany) running at an operating pressure of 10^{-9} mbar was used for ToF-SIMS in-depth profiling. A pulsed 25 keV Bi^+ primary ion source delivering a 1.2 pA current over a 100×100 μm^2 area was adopted for analysis, and a 2 keV Cs^+ giving a 100 nA target current over 300×300 μm^2 area was used for sputtering. For better sensitivity to the oxide species, the analysis was performed in the negative mode. The Ion-Spec software was used for data

acquisition and post-processing analysis. XPS analysis was performed using a Thermo Electron Escalab 250 spectrometer with a monochromated Al Kα radiation (hν= 1486.6 eV) running at operating pressure around 10^{-9} mbar. The pass energy settings were 50 eV for survey spectra and 20 eV for high resolution spectra. Thermo Avantage software (Version 5.956) was used for recording and for spectra analysis.

3. Results and discussion

3.1 Influence of 0.1 M 5-S-Sal in NaCl electrolyte on corrosion behavior of pure Mg

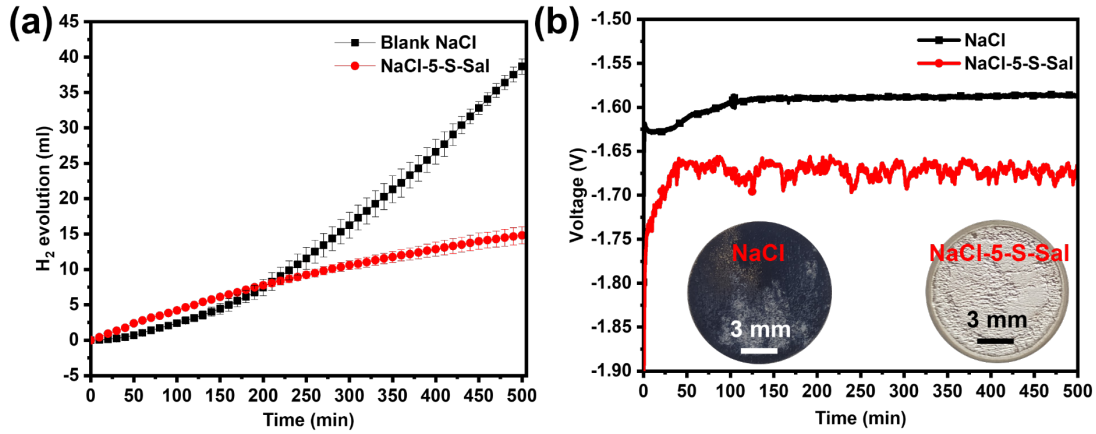

Fig. 1 Mg anode in 0.6 M NaCl electrolyte without and with 0.1 M 5-S-Sal (a) H_2 evolution test at open circuit potential (OCP) (b) OCP measurements and digital camera images of Mg samples after 300 min of immersion.

First, the corrosion behavior analysis of pure Mg samples in NaCl electrolyte with and without inhibitor using the hydrogen evolution tests at OCP, LSV and EIS are demonstrated. The H_2 evolution reflects the corrosion rate of metallic Mg according to reactions (1 and 2), where a dissolution of 1 mol of Mg generates 1 mol H_2 [8, 16, 26]. Fig. 1a shows the H_2 evolution at OCP in 0.6 M NaCl with or without inhibitor and Fig.

1b is the corresponding OCP. In electrolyte without inhibitor, H_2 evolution shows a slow augmentation up to around 100 min, and then, the quasi exponential increase during the following 400 min of immersion. OCP curve also demonstrates an increase to -1.54 V (*vs* Ag/AgCl) during around 100 min of immersion. The OCP increase can be attributed to the cation adsorption (*e.g.* H_3O^+) on the Mg electrode surface, which potential of zero charge is more negative than its equilibrium potential [27]. Interestingly, with the first 100 min of H_2 evolution and potential increases, the concomitant development of black corrosion spots on the Mg electrode surface can be observed. The Mg electrode surface becomes almost fully covered by the black corrosion spots during this time of immersion (the left-hand inset of digital camera image in Fig. 1b). The corrosion spots can catalyze the hydrogen evolution reaction (HER) [28, 29], which can explain the exponential increase of H_2 volume in Fig. 1a. Then, after 100 min, the OCP value stabilizes at around -1.56 V due to the equilibrium between the cation adsorption on Mg surface and full surface coverage by dark corrosion spots.

With 0.1 M 5-S-Sal inhibitor in the electrolyte, the stable OCP is reached at -1.68 V, which is 120 mV lower than in the blank NaCl electrolyte. More negative OCP of Mg in half cell configuration is beneficial for achieving a higher discharge potential in full Mg-air battery [26]. Although the volume of H_2 evolution is slightly higher in presence of inhibitor in electrolyte during the first 150 min, the linear and not exponential increase is observed in the following minutes of immersion resulting in around 13 ml of H_2 in comparison to almost four-fold volume of H_2 (40 ml) in a blank electrolyte at

the end of immersion tests (500 min). It was previously explained that 5-S-Sal inhibits the corrosion process on Fe-containing intermetallics and Fe impurities present in Mg sample and increases the solubility of $Mg(OH)_2$ leading to significant decrease of precipitates and dark corrosion spots formation [30], as it can be confirmed by the image of bright Mg surface in the inset of Fig. 1b (right-hand image). The 5-S-Sal inhibitor can produce soluble complexes with Mg^{2+} of mild stability (log K_{Mg2+} is 5.1) [24, 31]. As cathodic inhibitor, it has the ability of complexing Fe^{3+} (Log KFe_{3+} = 36.8). These properties can lead to significant improvement in Mg corrosion behavior and keep the Mg surface clean from dark corrosion spots. Consequently, the anodic and cathodic reactions of Mg dissolution [32-35] and HER, respectively, are significantly slowed down.

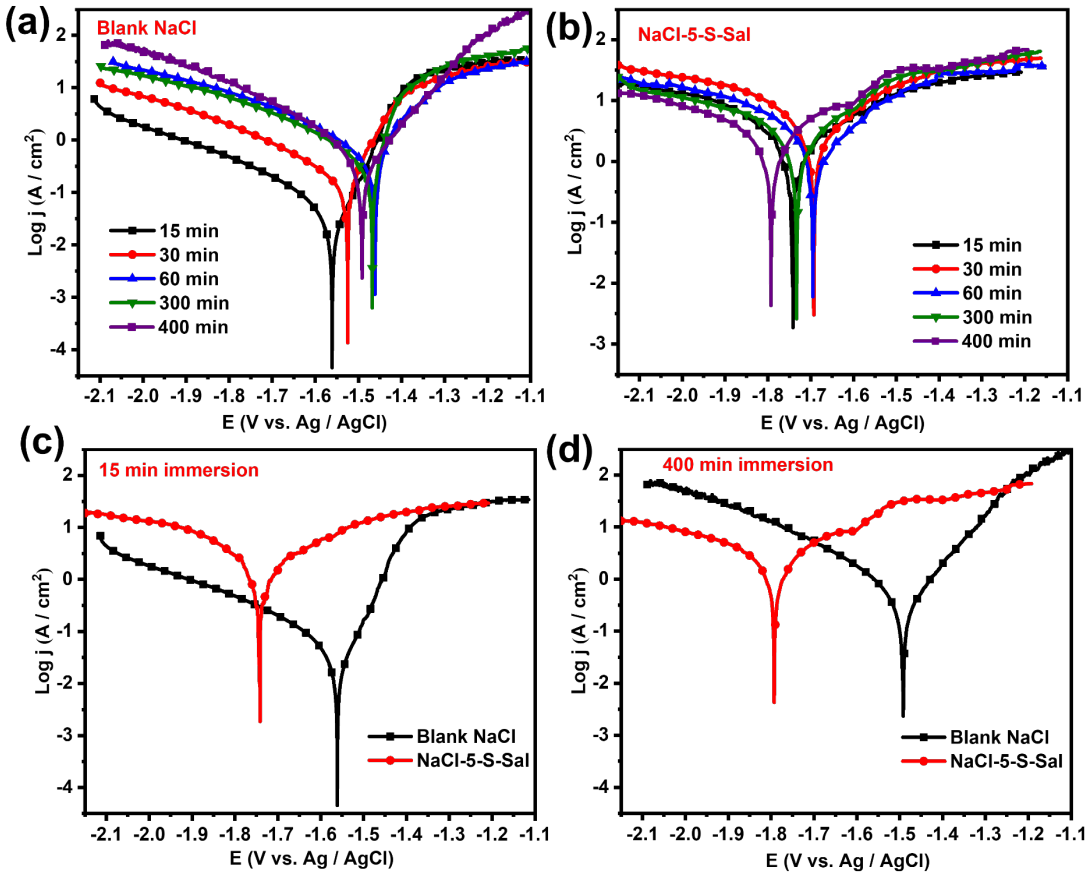

Fig. 2 LSV curves of Mg after different immersion times (15, 30, 60, 300 and 400 min) (a) in blank 0.6 M NaCl electrolyte (b) in 0.6 M NaCl electrolyte with 0.1 M 5-S-Sal inhibitor (c) comparison of 15 min immersion time (d) and 400 min immersion time in the two electrolytes.

To better understand the influence of 5-S-Sal inhibitor on the corrosion performance of Mg anode, potentiodynamic polarization curves (LSV) and electrochemical impedance spectroscopy were performed (Fig. 2 and Fig. 3, respectively) after different immersion times (15, 30, 60, 300 and 400 min).

The cathodic reaction corresponds to the hydrogen evolution reaction according to equation (1) and the anodic to Mg dissolution (2):

Cathodic reaction: $2H_2O+2e^- \rightarrow H_2 \uparrow +2OH^-$ (1)

Anodic reaction: $Mg \rightarrow Mg^{2+} + 2e^-$ (2)

These cathodic and anodic reactions correspond respectively to the cathodic and anodic branches of the polarization curves presented in Fig. 2. In blank NaCl (Fig. 2a), the increase of cathodic current density with immersion time indicates the augmentation of hydrogen evolution. As discussed above, the HER is catalysed by formation of dark corrosion spots [36], which formation can be easily observed on Mg electrode (as observed after immersion at OCP in Fig. 1b and Fig. 4). With the inhibitor (Fig. 2b), the cathode branch curves change scarcely as a function of immersion time indicating a stable corrosion behaviour of Mg anode. More significant slopes of the anodic branches in blank electrolyte (around 60 mV/decade) than in electrolyte with addition of 5-S-Sal inhibitor (around 20 mV/decade) are noticed. The higher Tafel slope denotes important dissolution of Mg anode (Fig. 2a). This behaviour is less pronounced for longer immersion times and more particularly in the electrolyte with inhibitor addition (Fig. 2 a, b). In order to better see the influence of inhibitor on cathodic and anodic behaviour of Mg after short (15 min) and long (400 min) time of immersion, the LSV curves were superimposed (Fig. 2 c and d). Fig. 2c shows up a much flatter anodic branch for electrolyte with inhibitor than blank electrolyte for 15 min of immersion. The limiting anodic current density remained almost unaltered with the presence of inhibitor at different times of immersion (Fig. 2b). It means that the surface of Mg anode is less active and better protected in the presence of 5-S-Sal inhibitor over different immersion times. Moreover after 400 min of immersion (Fig. 2 d), the cathodic current, higher in electrolyte with 5-S-Sal at lower immersion times, decreases significantly,

indicating much lower cathodic activity and lower HER than in blank electrolyte.

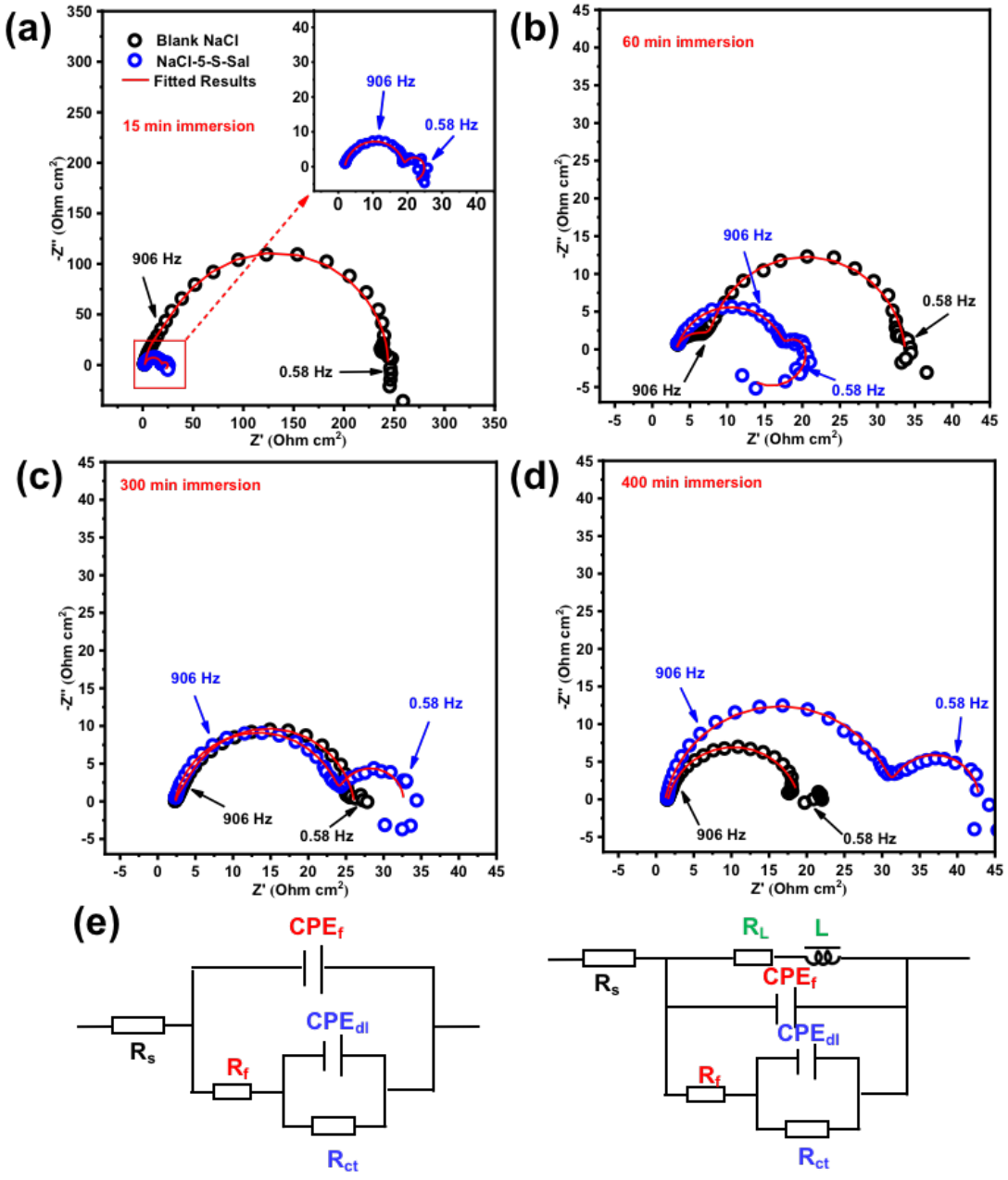

Fig. 3 Electrochemical impedance spectra of Mg anode in blank 0.6 M NaCl without and with and 0.1 M 5-S-Sal inhibitor after different times of immersion (a) 15 min (b) 60 min (c) 300 min (d) 400 min (e) equivalent circuits used for fitting the impedance spectra.

Table.1 Parameters obtained from the EIS data fitting for Mg anode in blank 0.6 M NaCl (NaCl) and in 0.6 M NaCl with 0.1 M 5-S-Sal inhibitor (NaCl-5-S-Sal).

	NaCl				NaCl-5-S-Sal			
	15 min	**60 min**	**300 min**	**400 min**	**15 min**	**60 min**	**300 min**	**400 min**
R_s (Ω cm^2)	12	3	2	2	11	10	11	2
R_{ct} (Ω cm^2)	74	6	4	2	17	15	22	30
CPE_{dl} (Ω^{-1} cm^{-2} s^n)	8×10^{-6}	75×10^{-6}	0.2×10^{-3}	0.6×10^{-3}	23×10^{-6}	48×10^{-6}	46×10^{-6}	49×10^{-6}
n_1	1	0.80	0.93	0.86	0.88	0.84	0.88	0.87
R_f (Ω cm^2)	167	25	20	15	6	3	8	11
CPE_f (Ω^{-1} cm^{-2} s^n)	13×10^{-6}	0.2×10^{-3}	0.3×10^{-3}	0.3×10^{-6}	13×10^{-3}	16×10^{-3}	11×10^{-3}	11×10^{-3}
n_2	0.99	0.99	0.86	0.86	0.92	0.93	1	1
L (H)	/	/	/	/	150	32	/	/
R_L (Ω cm^2)	/	/	/	/	39	14	/	/

Fig. 3 shows the electrochemical impedance spectra performed at free corrosion potential after various immersion times and the equivalent circuits used for fitting the experimental data. The Nyquist plots show high and low-frequency loops. The capacitive loop at the high-frequency range with a charge transfer resistance (R_{ct}) and a double capacitance (CPE_{dl}), corresponds to the reactivity at the electrolyte / metallic substrate interface [37-41]. Another capacitive loop at the low-frequency range with a film resistance (R_f) and the capacitance (CPE_f) can be attributed to the reactivity of the film (surface layer) [42]. The constant phase elements (CPE) were usually adopted for fitting, to substitute the ideal capacitors in both frequencies (for n equals to 1, the CPE is a pure capacitor) [43, 44]. This deviation from the ideal dielectric behavior can be explained by a heterogenous and rough surface of the Mg electrode [39-41]. As shown in Table 1, the n_1 is usually lower than 1 and the values closer to 1 can be observed for

n_2 in electrolyte with inhibitor indicating less rough and more homogenous films. For Mg exposed to electrolyte with inhibitor, the fairly resolvable corrosion products on Mg surface leads to appearance of the third time constant at low frequencies with an inductive loop. In the case of electrolyte without inhibitor, the scatter plot can be observed at these frequencies indicating less stable non-stationary conditions due to significantly rougher surface layer with a possible corrosion product flaking. The EIS spectra were fitted using the equivalent circuit shown in Fig. 3e [45-49], the left part for Mg in blank NaCl and the right part for Mg in the electrolyte with inhibitor (15 and 60 min).

The fitting parameters (Table 1) show that the values of R_{ct} and R_f decrease in blank NaCl with immersion time particularly from 15 min to 60 min. These results corroborate with the polarization results, *i.e.* the significant changes in the beginning of immersion. However, in the electrolyte with the inhibitor, R_{ct} and R_f values vary much less as function of immersion time. The opposite tendency can be observed for the charge transfer resistance (R_{ct}): a decrease and an increase as a function of immersion time in blank electrolyte and in the electrolyte with the inhibitor, respectively. The higher R_{ct} values indicate a reactivity decrease at the electrolyte / metallic substrate interface. Besides, the CPE_{dl} increases with of immersion time and in the case of electrolyte with inhibitor the CPE_{dl} is rather stable. The Nyquist plots (Fig.3 a-d) show that the -Z'' in blank NaCl is far larger than in NaCl-5-S-S at 15 min, then very similar values can be observed at 300 min and finally -Z'' value declines in blank NaCl electrolyte. This is even more clear in the Bode spectra (Fig. S1) showing a significantly

higher values of log |Z| (0.9 Ω.cm^2) at low frequencies in comparison to 5-S-Sal inhibitor at 15 min, which turn to lower values (0.3 Ω.cm^2 at 400 min). These results denote that the inhibitors can greatly reduce the effect of immersion time on the corrosion of Mg anode which is beneficial to the long discharge performance of Mg-air batteries.

3.2 Mg surface degradation induced by immersion tests

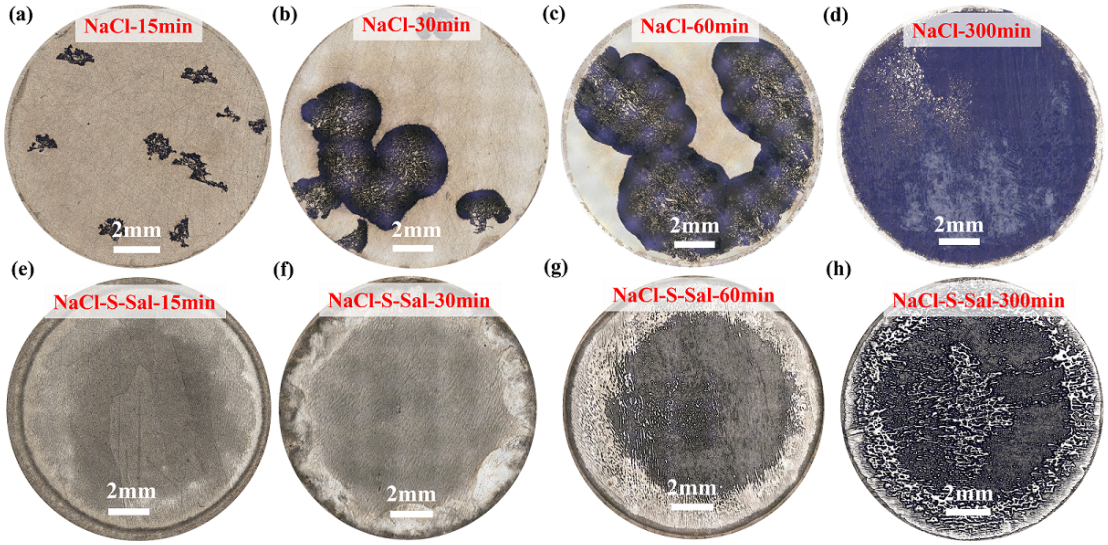

Fig. 4 Optical microscope images after different immersion times in 0.6 M NaCl electrolyte without (upper raw) and with 0.1 M S-Sal inhibitor (lower raw) (a) (e) 15 min, (b) (f) 30 min, (c) (g) 60 min, (d) (h) 300 min.

Fig. 4 presents the optical microscopy images of Mg anode after different immersion times in electrolyte without or with 5-S-Sal inhibitor. In the blank NaCl electrolyte (Fig. 4a-d), the obvious dark and non-reflective areas progressively grow on the Mg surface to finally cover the entire Mg electrode. However, there are not such dark corrosion spots on the surface immersed in 5-S-Sal additive (Fig. 4e-h and digital pictures in the

insets of Fig. 1b), instead, the surface became rougher as time of immersion increases. As the hydrogen evolution is observed to evolve principally in the dark areas [16, 50], it can be confirmed from these optical images that the corrosion of Mg is significantly decreased in the electrolyte with inhibitor.

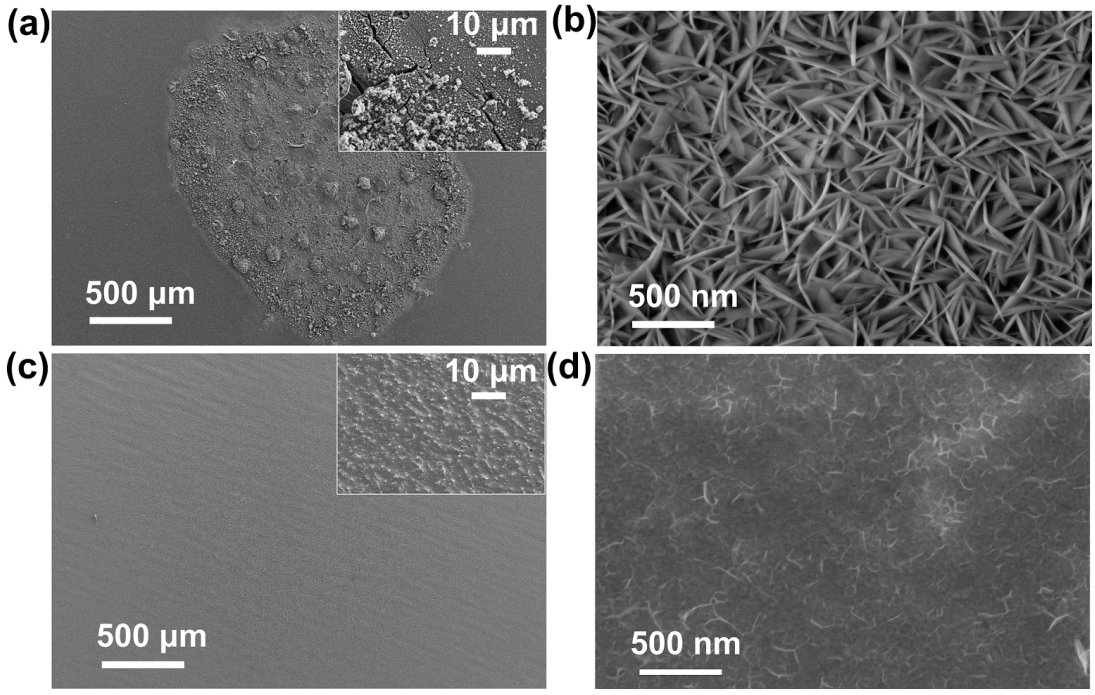

Fig. 5 SEM image of surface morphologies of Mg anode after 15 min immersion at OCP (a) in a blank 0.6 M NaCl electrolyte, (inset presents the magnified rough surface area corresponding to dark corrosion spots) (b) the magnified image of areas out of black corrosion spots (bright parts shown in optical microscopy in Fig. 4) (c) in 0.6 M NaCl with 0.1 M 5-S-Sal inhibitor (d) the magnified image of sample present in c.

As shown by SEM, in blank NaCl (Fig. 5 a), the surface of Mg electrode is very heterogenous with areas of severe corrosion corresponding to black corrosion spots. These corrosion spots show also a cracked layer (inset image in Fig. 5 a). However, with the addition of 5-S-Sal inhibitor, a homogeneous surface layer can be observed at

a micrometric level (Fig. 5 c). It indicates that 5-S-Sal inhibitor reduces the severe Mg corrosion and limits the formation of dark areas catalyzing the HER [28, 29]. However, the development of porous structures with characteristic nanoplatelets of magnesium oxide-hydroxide layer [51] can be observed in the areas out of black corrosion spots in both electrolytes (Fig. 5 b and d). A lower porosity and less developed flake-like structure are observed on the surface exposed to electrolyte containing 5-S-Sal inhibitor. One hypothesis is that 5-S-Sal inhibitor prevents the formation of porous structure $Mg(OH)_2$ layer by adsorption of the organic molecules (*e.g.* inhibitor) on the Mg surface [30, 32] and another one that the 5-S-Sal can induce a dissolution of hydroxide and/or precipitates. A mixed function of inhibitor cannot be ruled out and it will be discussed here below.

3.3 Influence of 5-S-Sal inhibitor in NaCl electrolyte on discharge performance of Mg-air battery

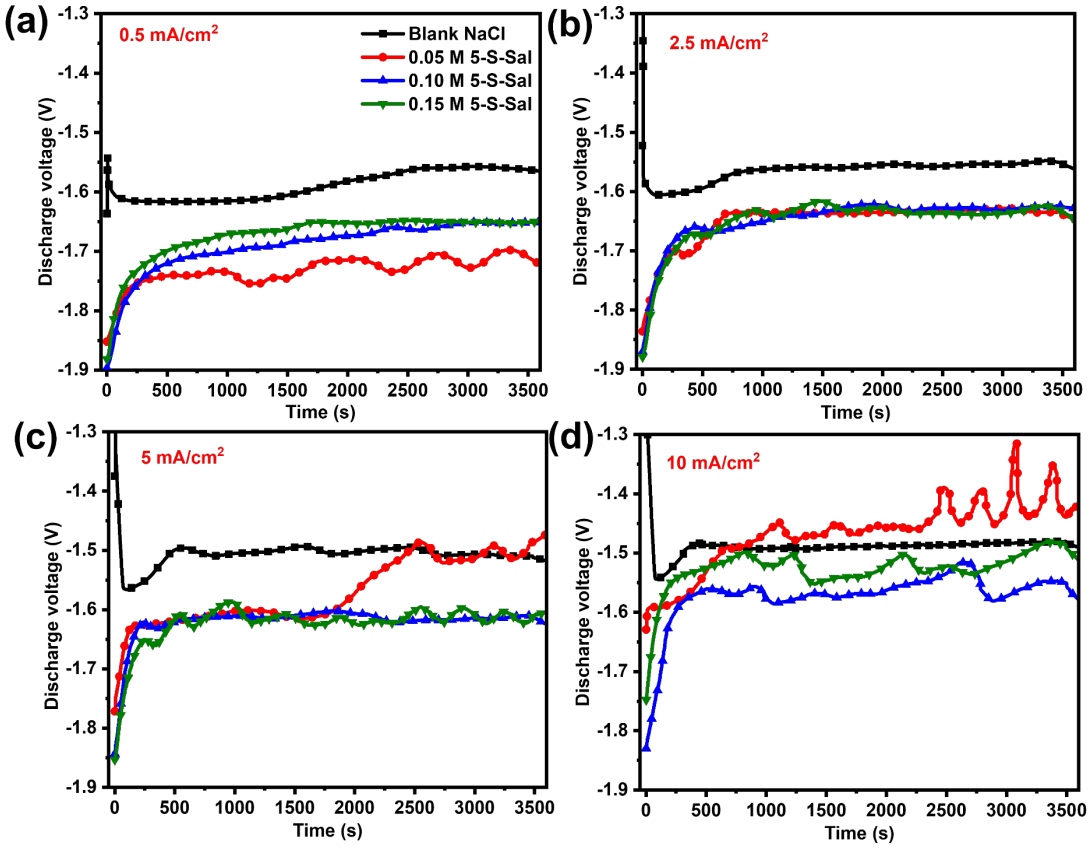

Fig. 6 Discharge performance of half Mg-air battery cells in blank 0.6 M NaCl and with 0.05 M, 0.1 M and 0.15 M 5-S-Sal inhibitor at different current densities (a) 0.5 mA/cm^2, (a) 2.5 mA/cm^2, (a) 5 mA/cm^2, (a) 10 mA/cm^2.

Following the promising results obtained on Mg corrosion with 5-S-Sal inhibitor in NaCl electrolyte, a series of discharge tests of Mg-air battery in half and full cell configurations were performed. Fig.6 presents the half-cell discharge performance of Mg in blank NaCl electrolyte with various concentration of 5-S-Sal (0.05, 0.1 and 0.15 M) at different current densities (0.5, 2.5, 5, and 10 mA/cm^2). In blank NaCl electrolyte at different current densities, the discharge potential decreases immediately and then increases to a stable value, which can be attributed to a native oxide breakdown, the attack of Mg (dissolution) and rapid formation of a corrosion product layer. In the

electrolyte with 5-S-Sal inhibitor, the discharge voltage increases slowly from the low potential (equivalent to OCP value of around -1.8 V, as also shown in Fig. 1b) to the stable value and it can be explained by a slow layer growth, which is influenced by the reactivity of inhibitor at the electrolyte/metal interface (*e.g.* inhibitor adsorption on Mg surface). A slower kinetics of surface film growth is consistent with a more stable behavior observed by EIS (Fig. 4) and less significant morphological surface modifications demonstrated by SEM (Fig. 5b). At 0.5 mA/cm^2 (Fig. 6 a), the most negative discharge potential for Mg is detected in 0.05 M 5-S-Sal. At 2.5 mA/cm^2 (Fig. 6 b) the same and stable discharge potential of -1.63 V is observed for all inhibitor concentrations. This potential is more negative than those observed in the blank NaCl electrolyte (-1.55 V). However, at higher current densities of 5 mA/cm^2 (Fig. 6 c), in electrolyte with the lower inhibitor concentration (0.05 M), an unstable discharge potential is observed (a potential jump at around 1750 s). In the same electrolyte, at higher current density discharge (10 mA/cm^2 in Fig. 6 d), the potential increase and its important fluctuation can be observed. At 10 mA/cm^2 the discharge potentials, are similar regardless of inhibitor concentration. Thus, it can be concluded that the addition of inhibitor at certain concentrations (not less than 0.1M) is beneficial for Mg discharge voltage when the low current densities are applied.

The half-cell's discharge voltage [24] can be expressed as:

$$E_{anode} = E_{ocp} - \eta_{ct} - \eta_{diff} - IR \quad (3)$$

where the E_{ocp} is the open circuit potential, η_{ct} and η_{diff} represent the potential drops, due to charge transfer process and diffusion overpotential, respectively, caused by

discharge products. I and R are the loaded current and resistance of electrolyte between reference and working electrode [52-54]. Following this expression, it is clear that more negative OCP will contribute to lower discharge voltage assuming no modifications of other factors [17, 54, 55]. Furthermore, the clean Mg electrode with less corrosion products blocking the surface in electrolytes with inhibitor can lead to the lower resistance of electrolyte between working electrode (Mg) and reference electrode and consequently to the smaller potential drop. The close discharge voltages at higher current densities (Fig. 6 d) can be significantly influenced by IR drop but also by diffusion overpotential and charge transfer process. Summarizing these results, the optimal concentration of inhibitor for stable electrode behavior and discharge performance at different current densities is 0.1 M 5-S-Sal. For this reason, the battery performances in full cells and surface chemistry of Mg electrode in this electrolyte will be further studied in more details.

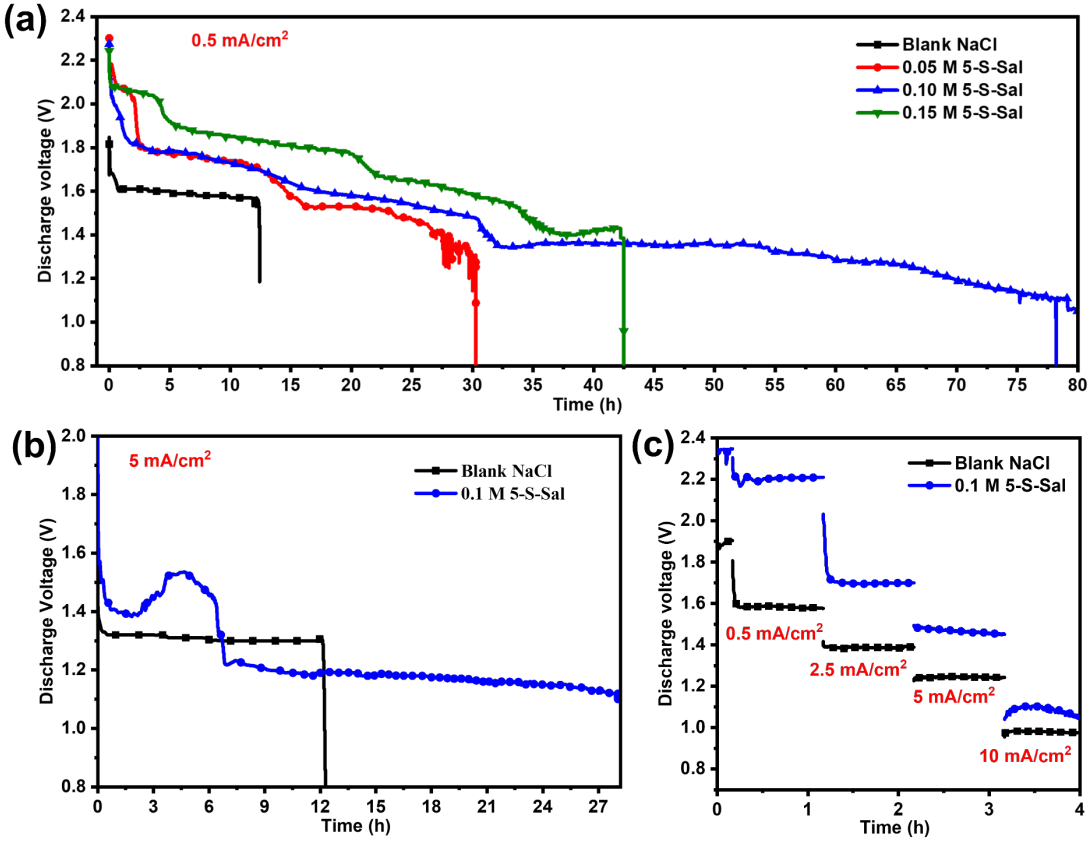

Fig. 7 Discharge curves of full Mg-air batteries obtained (a) in blank 0.6 M NaCl and with different concentration of 5-S-Sal electrolyte at current density of 0.5 mA/cm^2 for a long-time test, in blank NaCl and with 0.1 M 5-S-Sal inhibitor for comparison (b) at different current densities, (c) at current density of 5 mA/cm^2.

The discharge performances of full Mg-air batteries in electrolytes with or without inhibitors are presented in Fig. 7. The discharge voltage drops significantly after ~12.5 hours in blank NaCl (Fig. 7 a) and a serious corrosion damage and formation of large dark corrosion spots/holes were observed by eye on Mg plates. They can be attributed to the severe localized corrosion [56, 57] and local presence of other metallic inclusions and impurities such as Fe, Mn, as previously reported [23, 58]. In presence of 0.05, 0.15, and 0.1 M 5-S-Sal, the discharge times can be prolonged up to 30, 42, and 80

hours, respectively (Fig. 7a). It indicates that the inhibitors can greatly increase the service time of Mg plates, which can be explained by a significant decrease of Mg corrosion. Moreover, the discharge voltage in presence of inhibitor is higher by 275-470 mV than in blank NaCl electrolyte (Fig. 7 a), which can be attributed to the superior OCP and more homogenous surface that can reduce the influence of overpotentials (according to equation 3). It should be noticed that there is a concentration threshold, which allows to obtain the best discharge performances most probably related to the optimized electrode/electrolyte interface properties. At higher current densities such as 5 mA/cm^2 (Fig.7 b), the lifetime of Mg is significantly prolonged in presence of 0.1 M 5-S-Sal (28 hours in comparison to 12 hours in NaCl without inhibitor). Unfortunately, the discharge potential is not stable during the first hours and drops to 1.2 V after 6 hours. The 5-S-Sal can be consumed by continuous complexing with Mg^{2+} as a function of time and thus the advantage of inhibitors is reduced. Furthermore, the influence of different current densities on discharge curves in two electrolytes is demonstrated in Fig. 7c. In presence of inhibitors, the discharge potential is higher by about 620 mV (at 0.5 mA/cm^2), 310 mV (at 2.5 mA/cm^2), 230 mV (at 5 mA/cm^2) and 130 mV (at 10 mA/cm^2) with reference to the blank NaCl electrolyte. It indicates that the efficiency of inhibitor decreases slightly at higher current densities. The reaction of complexing with Mg^{2+} or other ions (*i.e.* metallic impurities) [24], for which 5-S-Sal inhibitor is responsible, can be the rate-limiting step. To efficiently protect the Mg surface and keep the surface free of black corrosion spots, a stronger complexation ability and faster kinetics are necessary. In order to demonstrate a beneficial effect of the inhibitor the

utilization efficiency of Mg anode and energy efficiency in NaCl-based electrolyte with and without inhibitor were calculated following the procedure described in [24]. The discharge voltage was tested at 5 mA/cm^2. The utilization efficiency increases from 21 % to 36 % and the energy density from 608 to 1252 Wh/kg in blank NaCl electrolyte and NaCl electrolyte containing 5-S-Sal inhibitor, respectively. This utilization efficiency is higher than the recently reported utilization efficiency of 27 % of pure Mg anode (200 ppm Fe) measured at 0.5 mA/cm^2 in NaCl electrolyte with salicylate [23]. The utilization efficiency depends on the different contributions of self-corrosion and the chunk effect. The increased utilization efficiency can be related to decreasing the chunk effect (lowering the formation of metallic chunks and metal spalling). Although, the specific energy in doubled in electrolyte with inhibitor, this value is lower than the specific energy reported for Mg-based alloys used as negative electrodes in Mg-air batteries applying electrolytes with additives (corrosion inhibitors) [24]. It can be then interesting in future works to find a suitable Mg-based anode alloy in order to test the influence of 5-S-Sal inhibitor in NaCl electrolyte.

3.4 Influence of inhibitor on chemical composition of the surface layer on Mg anode

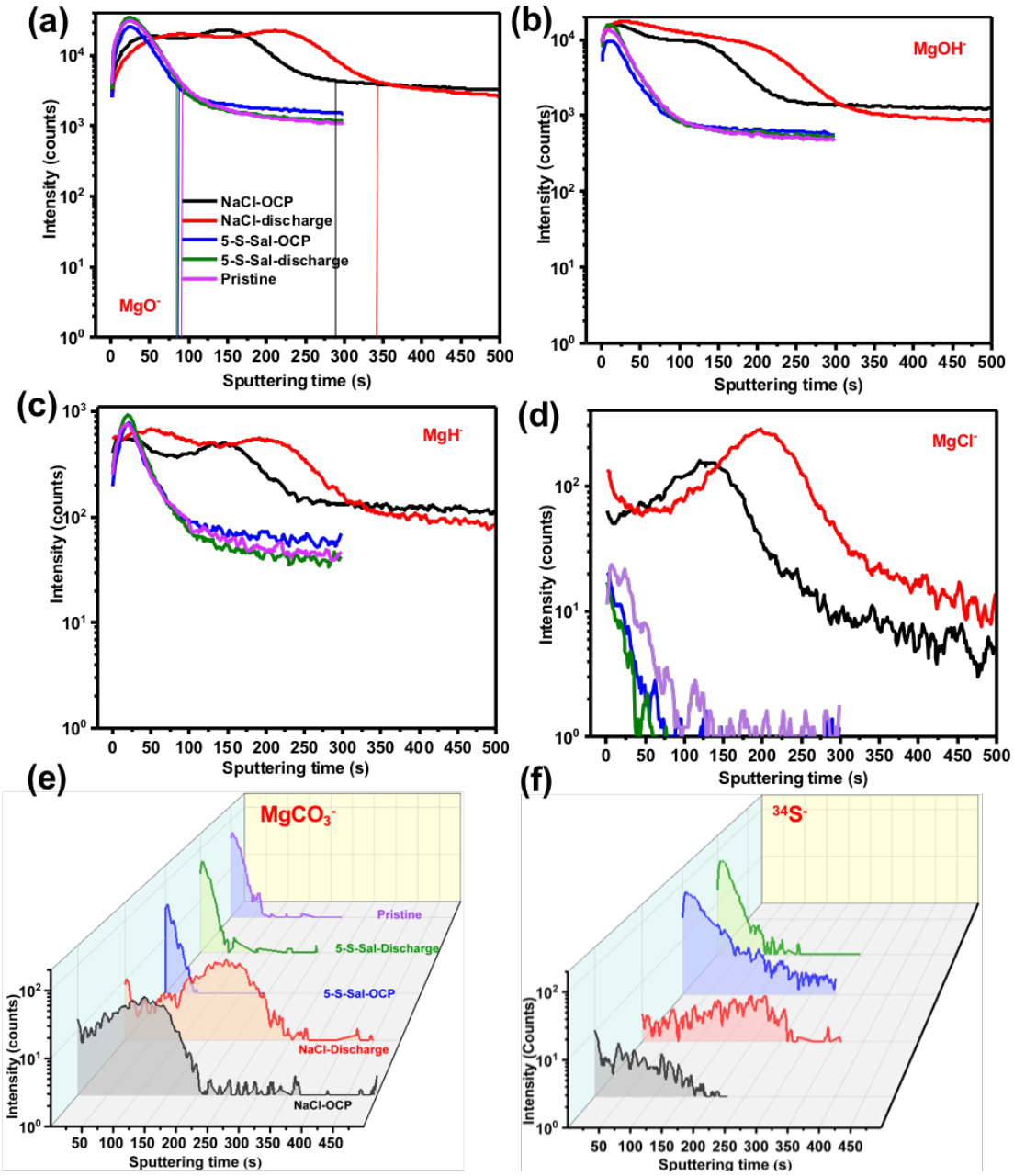

Fig. 8 ToF-SIMS (negative ions) in-depth profiles for the layers formed on the pristine Mg after polishing and after 15 min of immersion at OCP and discharge (full cell) in 0.6M NaCl electrolyte without and with 0.1 M 5-S-Sal inhibitor: (a) MgO^-, (b) $MgOH^-$, (c) MgH^-, (d) $MgCl^-$, (e) $MgCO_3^-$, (f) $^{34}S^-$.

To better understand the working mechanism of 5-S-Sal inhibitor in NaCl electrolyte, chemical characterization was performed by ToF-SIMS negative ion depth profiles (Fig. 8 and Fig. S2) after immersion at OCP and discharge tests of full Mg-air batteries. MgO^-, $MgOH^-$, MgH^-, $MgCl^-$, $MgCO_3^-$ ions [59] correspond to components of the passive or corrosion layer composition (magnesium oxide, hydroxide, hydride, chloride and carbonate, respectively) and $^{34}S^-$ ion to the presence of 5-S-Sal inhibitor. The very fast ion signal intensity increase observed during the first tens of seconds of sputtering corresponds to the time needed to reach the stationary conditions. The 80 % of maximum intensity of MgO^- signal decrease was used to define the position of the metal/oxide interface [60]. Based on the sputtering rate (0.1 nm/s estimated in our previous work [60]), the thickness of the layer formed on Mg surface in NaCl blank electrolyte is ~27.5 nm after immersion at OCP and ~33.5 nm after discharge test. First of all, it should be noted that the layers are much thicker than on the pristine electrode (~7.8 nm) indicating a significant growth of the oxide/hydroxide. Moreover, the thicker layer after discharge than after OCP indicates that the Mg dissolution and deposition of corrosion products is enhanced by the applied current indicating the increased chunk effect. In the electrolyte containing the inhibitor (after OCP and discharge), the thickness of the layer is almost the same (~7.5 nm) as on the pristine Mg sample, which indicates much lower Mg corrosion when the inhibitor is present. Interestingly, the intensity of the MgO^- signal for Mg samples exposed to the electrolyte with inhibitor is higher than for the blank NaCl electrolyte, in contrast with the $MgOH^-$ signal intensities. This indicates that the inhibitor favors the formation of MgO over $Mg(OH)_2$. These

results corroborate also with SEM (Fig. 5d), showing less flake-like porous structure typical of $Mg(OH)_2$. The lower $^{18}OH^-$ and higher ^{18}O signals (Fig. S2 a) in electrolytes with inhibitor agree well with this conclusion. Comparing the maximum intensity of MgO^-, $MgOH^-$ and MgH^- (Fig. 8 a, b and c) signals, it can be concluded that the MgH^- maximum is located between MgO^- and $MgOH^-$ (as clearly viewed after superposition of all these signals for each sample in Fig. S3). This indicates a multilayer structure of the film with magnesium hydrides embedded into magnesium hydroxide present on the extreme surface and the magnesium oxide present in the inner part of the layer, close to the interfacial region, as already reported by Seyeux *et al*. [59]. A high intensity $MgCl^-$ signal in blank NaCl electrolyte is observed within the whole thickness of the oxide/hydroxide layer, and particularly at the interface with the metallic substrate. Consequently, the high quantity of $Mg(OH)_2$, MgH_2 and/or $MgCl_2$ can catalyze the HER [28, 29] and enhance the rates of hydrogen evolution [61]. With 5-S-Sal inhibitor, the $MgCl^-$ signal is significantly weaker, close to the value observed for the pristine sample, and its intensity drops almost to zero in the interfacial region. This quasi absence of $MgCl^-$ species (representative of corrosion in chloride solution) confirms the efficient inhibition of Mg corrosion.

Besides, the S^- signal, which is a fingerprint of the sodium 5-sulfosalicylate molecule, is detected on Mg electrodes exposed to the electrolyte with inhibitor. As expected, a much higher S^- signal intensity (10 times) for Mg samples immersed at OCP or after discharge tests is observed for Mg surfaces exposed to electrolyte with inhibitor than without (Fig. 8 f). Apart the complexation effect of 5-S-Sal as described above [24, 31],

the presence of sulfur can lead to corrosion inhibition of Mg according to our group's study [58] showing the sulfur adsorption (S_{ads}(Fe)) on Fe-rich sites, which are the catalytic sites for the HER.

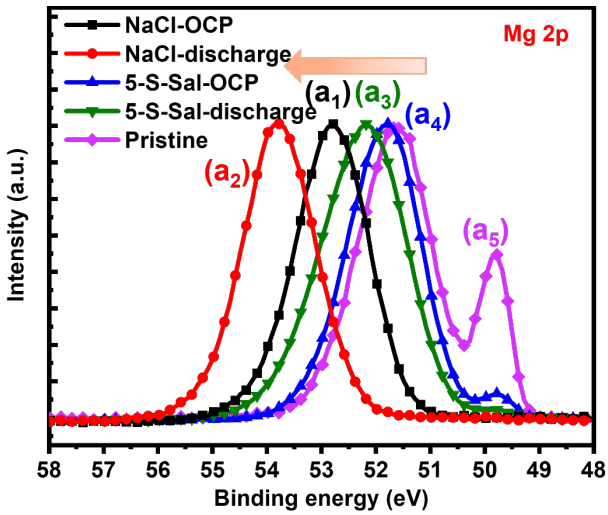

Fig. 9 XPS Mg 2p core level spectra for Mg anode in 0.6 M NaCl without or with 0.1 M 5-S-Sal inhibitor: (a_1) (a_3) after 15 min OCP, (a_2) (a_4) after 15 min discharge test (full cell), (a_5) Mg pristine after polishing

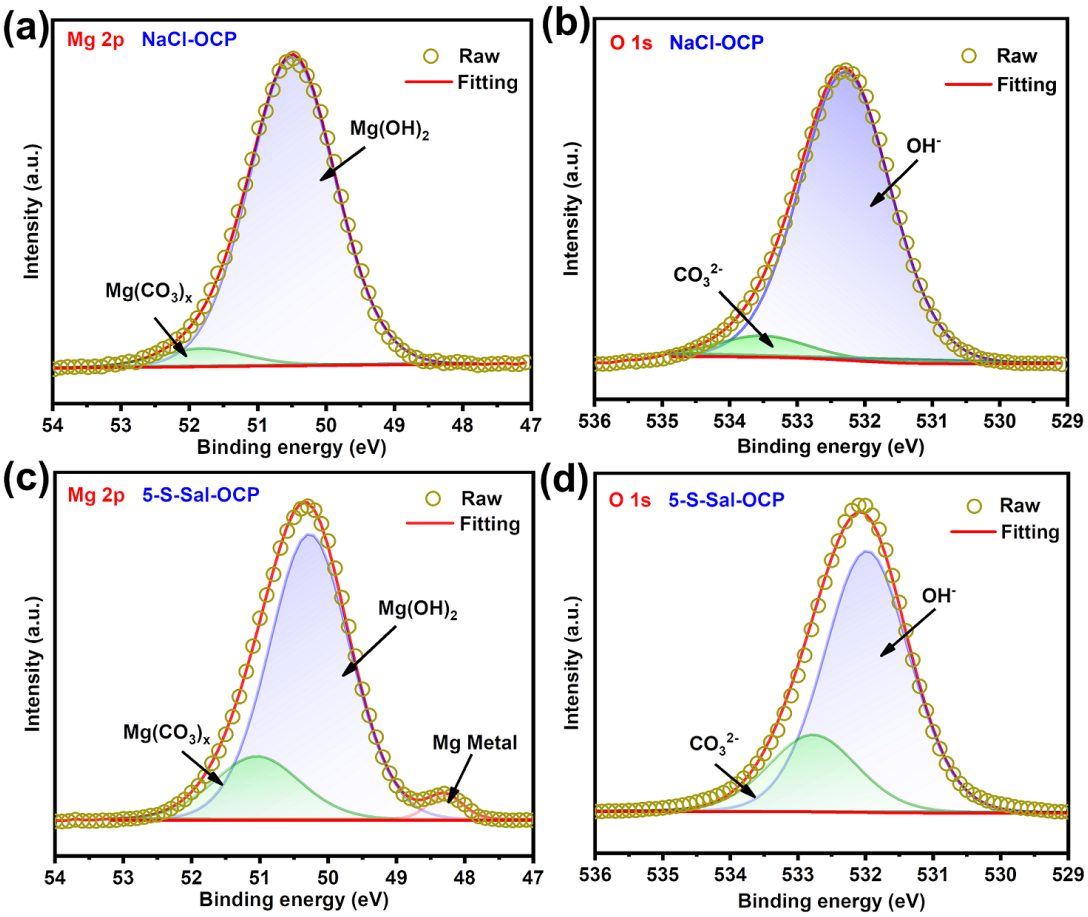

Fig. 10 XPS Mg 2p and O1s core level spectra for Mg anode after 15 min of discharge at a current density of 0.5 mA/cm^2 in (a) (b) blank 0.6 M NaCl electrolyte, (c) (d) 0.6M NaCl with 0.1 M 5-S-Sal inhibitor.

Table 2. Atomic % of Mg2p and binding energies of Mg 2p and O1s for different magnesium compounds calculated from XPS for Mg samples exposed to 0.6 M NaCl electrolyte with 0.1 M 5-S-Sal and without inhibitor (at OCP and after discharge test at current density of 0.5 mA/cm^2).

Atomic% Mg 2p	NaCl-OCP	NaCl-discharge	5-S-Sal-OCP	5-S-Sal-discharge	Peak position Mg 2p (eV)	Peak position O 1s (eV)
Mg metal	/	/	3	/	49.8*	/
$Mg(OH)_2$	95	96	79	79	50.3 ± 0.2	532.1 ± 0.2
$MgCO_3$	5	4	18	21	51.3 ± 0.4	533.2 ± 0.3

* No correction for charging effects.

Fig. 9 a shows the XPS Mg 2p core level spectra for the pristine Mg sample and Mg anode exposed to 0.6 M NaCl electrolyte without and with 0.1 M 5-S-Sal inhibitor at OCP and after discharge tests in full cells. Two peaks can be clearly distinguished for the pristine sample (Fig. $9a_5$) and for the Mg sample immersed at OCP in the electrolyte with 5-S-Sal inhibitor (Fig. $9a_4$): a peak at 49.8 eV, attributed to metallic Mg, and the other peak at higher binding energy, which corresponds to the magnesium compounds as specified hereafter [41]. For other Mg samples (Fig. 9 (a_1), (a_2) and (a_3)), only one higher binding energy peak corresponding to compounds characteristic of corrosion layers are observed. This layer is too thick to detect the signal of metallic Mg, due to attenuation of the signal by the thick surface layer (probing depth of about 8 nm). Moreover, the Mg(II) components in the Mg 2p spectra show shifts towards higher binding energies, with reference to Mg 2p peak for pristine sample, of around +1.1 eV (after immersion at OCP), +2.1 eV (after discharge) in blank NaCl electrolyte and around +0.1 eV (after immersion at OCP), +0.5 eV (after discharge) in electrolyte with inhibitors. The more positive binding energy indicates a charge effect induced by formation of thicker or less conductive surface layers [58, 62]. Much less significant Mg 2p shift observed in case of Mg exposed to electrolyte with inhibitor (Fig. 9 (a_3)

and (a_4)) implies formation of much thinner layers. These results are consistent with the ToF-SIMS data presented above.

A decomposition of Mg 2p and O 1s spectra was performed to determine the species present in the oxide layers (Fig. 10 and Fig. S4). The binding energy was corrected using the position of the C 1s signal from hydrocarbons (-CH-CH-) (286 eV) [63]. Table 2 depicts different magnesium compounds, principally $Mg(OH)_2$ at 50.3 ± 0.2 eV, $MgCO_3$ at 51.3.± 0.4eV [64] and their corresponding atomic percentage calculated from Mg 2p spectra. The quantity of $Mg(OH)_2$ is reduced by almost half in 5-S-Sal-containing electrolyte as compared to blank NaCl electrolyte and an increase of $MgCO_3$ formation is observed leading to enhanced corrosion inhibition [65, 66]. The presence of $Mg(OH)_2$ and $MgCO_3$ in Mg 2p spectra is also confirmed by the decomposition of O 1s spectra (Fig. 10 b and d). The stoichiometry of these compounds was also calculated using the Mg 2p and O 1s peak intensities (corresponding to magnesium hydroxide or carbonate). The corrosion inhibition can be also governed by sodium 5-sulfosalicylate inhibitor, which presence is manifested by the S 2p signal (Fig. 11). The S 2p peak shows a spin-orbit doublet at 168.9 eV (S $2p_{1/2}$) and 167.7 eV (S $2p_{3/2}$) indicating the presence of -SO_3-, which corresponds to the inhibitor molecule [58, 67]. The sulfur species adsorbed on the Mg surface can reduce the anodic dissolution and hydrogen evolution as previously demonstrated [58]. The presence of S-containing species agrees also with ToF-SIMS data (Fig. 8f).

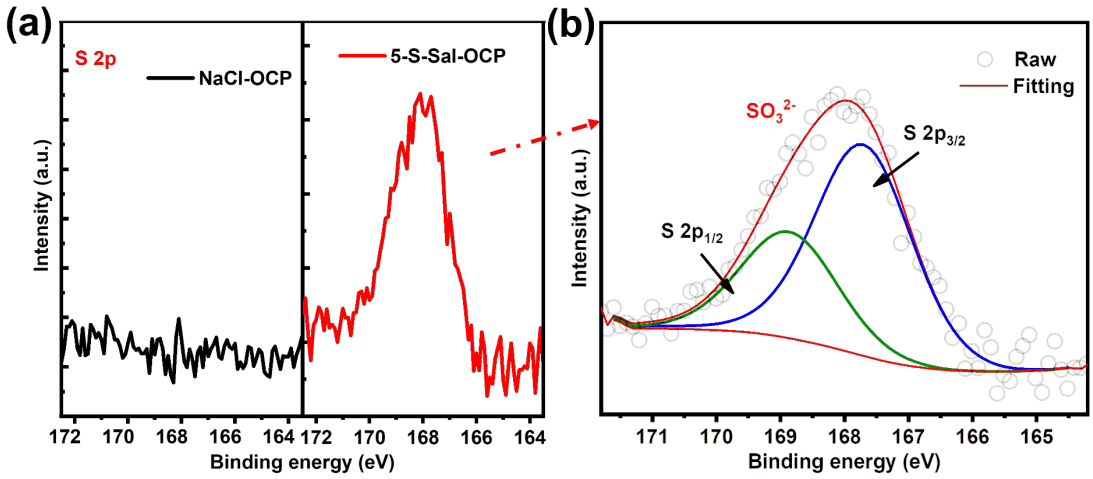

Fig. 11 (a) Comparison of S 2p core level spectra for Mg anodes in 0.6 M NaCl without or with 0.1 M 5-S-Sal inhibitor, (b) decomposition S 2p for Mg anode obtained in the electrolyte with 0.1 M 5-S-Sal.

3.5 Mg negative electrode degradation after discharge tests as a function of used electrolyte

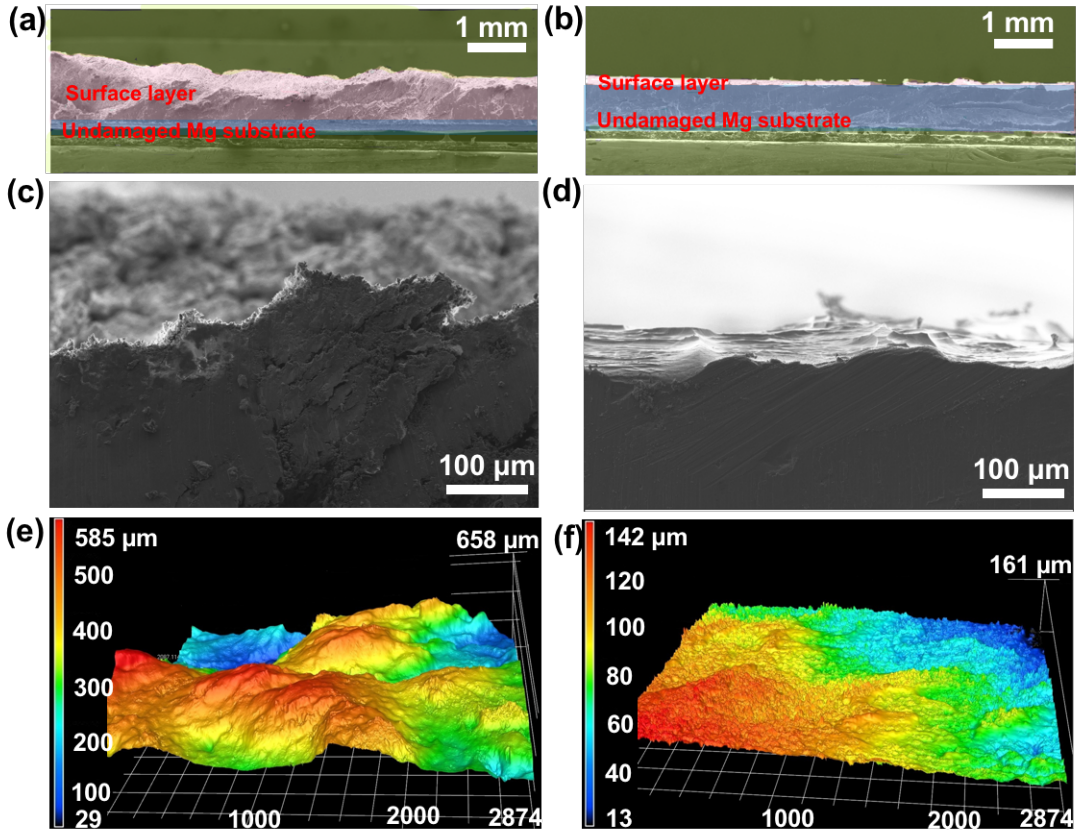

Fig. 12 Cross-section SEM images of Mg samples after 5 hours of discharge tests in (a and c) blank 0.6 M NaCl, (b and d) with 5-S-Sal inhibitor added to electrolyte. Three-dimensional topography laser microscope of Mg anode after 5 hours of discharge tests (full cell) (e) in blank 0.6 M NaCl, (f) in electrolyte with 5-S-Sal inhibitor.

To observe the in-depth modifications and degradations of Mg plates, SEM analyses were performed on Mg anodes after 15 min discharge test at a current density of 0.5 mA/cm^2 in full battery cell (Fig. S5). Apparently, several mm of diameter dark corrosion spots are present in the blank NaCl electrolyte (Fig. S5 a), whereas no dark spots appear on Mg anode discharged under the same conditions in the electrolyte with 5-S-Sal inhibitor. At the nanometric level (Fig. S5 b and d), it is shown that the discharge tests lead to formation of characteristic flake-like porous structure attributed

to magnesium oxide-hydroxide layer [51, 68] in blank NaCl electrolyte. The presence of inhibitor leads to formation of more homogenous layers without characteristic flake-like structure for the Mg samples i longer discharge time. These results are perfectly consistent with SEM observation of Mg after OCP tests (Fig. 5), which show no black areas when the inhibitor is added.

Cross-section SEM images of Mg after 5 hours of discharge tests (Fig. 12 (a-d)) show that the Mg samples are seriously damaged and the Mg electrode is almost completely consumed in blank NaCl electrolyte. However, only slight dissolution of Mg sample in electrolyte with 5-S-Sal inhibitor is observed, with a little enrichment in corrosion products on the surface (Fig. 12 c, d, respectively). Consistent with the 3D laser microscope images, much flatter surface topography (lower roughness) is observed (Fig. S6) for Mg anode in presence of inhibitor (322 μm and 443 μm for blank NaCl *vs* 34 μm and 31 μm with 5-S-Sal additive). It indicates that the 5-S-Sal inhibitor effectively prevents the pitting corrosion of Mg anode exposed to long time discharge test. Thus, the service time of Mg-air batteries can be greatly prolonged.

4. Conclusions

The influence of sodium 5-sulfosalicylate as an inhibitor in 0.6 M NaCl electrolyte on Mg-air battery performance and the stability of Mg electrode were thoroughly investigated by combining electrochemical, surface morphology and chemical surface characterization methods. The addition of sodium 5-sulfosalicylate as an inhibitor leads to the significant improvement of corrosion behavior of Mg and discharge performance of Mg-air battery by showing:

1) A more negative OCP and an improved average discharge voltage by 275-470 mV (during the discharge test of full cells at a current density of 0.5 mA/cm^2),
2) A much less active cathodic behavior of Mg electrode by linear sweep voltammetry measurements and a stable impedance value after long-time immersion,
3) A four-fold reduction of the hydrogen evolution in comparison to the blank electrolyte,
4) An improved discharge potential from ~1.58 V to ~1.82 V at current density of 0.5 mA/cm^2 and prolonged battery lifetime from ~12.5 hours to ~ 80 hours for the optimized inhibitor concentration of 0.1 M.
5) The increased utilization efficiency and a doubled energy density.

The improved corrosion and discharge properties in presence of inhibitor in electrolyte can be explained by different structure and composition of the surface film as demonstrated by ToF-SIMS and XPS:

1) A higher amount of MgO on the extreme surface and a lower amount of $Mg(OH)_2$ in the inner part of the multilayer structure. The magnesium hydrides were found to be embedded into magnesium oxide and hydroxide.
2) A lack of chlorides and a slight enrichment in sulfur species, which could be responsible for blocking the active, catalytic sites of HER. However, the effect of complexation of Mg^{2+} or other ions (*i.e.* metallic impurities) by 5-S-Sal inhibitor on the corrosion inhibition as previously demonstrated cannot be ruled out.

3) The formation of a layer with limited thickness, which can be related to the reduced chunk effect.

Following the promising results obtained in this work, the further studies can be focused on other Mg corrosion inhibitors (such as salicylaldehide, 3-Methylsalicylate Na, 2,5-pyridinedicarboxylate Na, 8-Hydroxyqeinoline) leading to a stronger complexation ability and faster kinetics, however, parallelly the studies should be also performed on Mg-alloys. Understanding the working mechanisms by a thorough analysis of the electrode/electrolyte interface is also unavoidable in development of the better Mg-air battery systems.

Acknowledgements

Région Île-de-France is acknowledged for partial funding of the ToF-SIMS equipment. Prof. Jun-Tao Li and Yao Zhou are acknowledged for discussion and suggestions in this project. The first author is grateful to the China Scholarship Council (CSC) for funding. (No. 201806310116).

References

[1] R. Kumar, S. Sahoo, E. Joanni, R.K. Singh, W.K. Tan, K.K. Kar, A. Matsuda, Recent progress in the synthesis of graphene and derived materials for next generation electrodes of high performance lithium ion batteries, Progress in Energy and Combustion Science, 75 (2019) 100786.

[2] R. Kumar, R.K. Singh, A.V. Alaferdov, S.A. Moshkalev, Rapid and controllable synthesis of Fe3O4 octahedral nanocrystals embedded-reduced graphene oxide using microwave irradiation for high performance lithium-ion batteries, Electrochimica Acta, 281 (2018) 78-87.

[3] L. Gaines, Lithium-ion battery recycling processes: Research towards a sustainable course, Sustainable Materials and Technologies, 17 (2018) e00068.

[4] G. Zubi, R. Dufo-López, M. Carvalho, G. Pasaoglu, The lithium-ion battery: State of the art and future perspectives, Renewable and Sustainable Energy Reviews, 89 (2018) 292-308.
[5] J. Światowska, P. Barboux, Lithium process chemistry. Resources, extraction, batteries and recycling. Chapter 4 – lithium battery technologies: from the electrodes to the batteries, Elsevier, pp (2015) 125-166.
[6] X. Feng, M. Ouyang, X. Liu, L. Lu, Y. Xia, X. He, Thermal runaway mechanism of lithium ion battery for electric vehicles: A review, Energy Storage Materials, 10 (2018) 246-267.
[7] R. Van Noorden, The Rechargeable Revolution: A Better Battery, Nature, 507 (2014) 26.
[8] T. Zhang, Z. Tao, J. Chen, Magnesium–air batteries: from principle to application, Mater. Horiz., 1 (2014) 196-206.
[9] B.J.I. M. Fichtner, E. Sheridan, R. Mohtadi, C. Battaglia, Z. Zhao-Karger, P. Canepa, R. Dominko, D. Hoeche, M. Weil, Magnesium Batteries: Research and Applications, Royal Society of Chemistry, (2019).
[10] E. Erdem, Why P2X must be the part of the energy solution?, Environmental Progress & Sustainable Energy, 40 (2020) ep.13545.
[11] A.M. S. S. Sharma, Towards more environmentally and socially responsible batteries, Energy Environ. Sci, 13 (2020) 4087-4097.
[12] X. Liu, J. Xue, The role of Al2Gd cuboids in the discharge performance and electrochemical behaviors of AZ31-Gd anode for Mg-air batteries, Energy, 189 (2019) 116314.
[13] Y. Li, X. Zhang, H.-B. Li, H.D. Yoo, X. Chi, Q. An, J. Liu, M. Yu, W. Wang, Y. Yao, Mixed-phase mullite electrocatalyst for pH-neutral oxygen reduction in magnesium-air batteries, Nano Energy, 27 (2016) 8-16.
[14] F. Cheng, J. Chen, Metal-air batteries: from oxygen reduction electrochemistry to cathode catalysts, Chem Soc Rev, 41 (2012) 2172-2192.
[15] M. Esmaily, J.E. Svensson, S. Fajardo, N. Birbilis, G.S. Frankel, S. Virtanen, R. Arrabal, S. Thomas, L.G. Johansson, Fundamentals and advances in magnesium alloy corrosion, Progress in Materials Science, 89 (2017) 92-193.
[16] G. Song, Recent Progress in Corrosion and Protection of Magnesium Alloys, Advanced Energy Materials, 7 (2005) 563-586.
[17] X. Chen, S. Ning, Q. Le, H. Wang, Q. Zou, R. Guo, J. Hou, Y. Jia, A. Atrens, F. Yu, Effects of external field treatment on the electrochemical behaviors and discharge performance of AZ80 anodes for Mg-air batteries, Journal of Materials Science & Technology, 38 (2020) 47-55.
[18] M. Deng, L. Wang, D. Höche, S.V. Lamaka, D. Snihirova, B. Vaghefinazari, M.L. Zheludkevich, Clarifying the decisive factors for utilization efficiency of Mg anodes for primary aqueous batteries, J Power Sources, 441 (2019) 227201.
[19] T. Zheng, Y. Hu, Y. Zhang, S. Yang, F. Pan, Composition optimization and electrochemical properties of Mg-Al-Sn-Mn alloy anode for Mg-air batteries, Mater Design, 137 (2018) 245-255.
[20] Y. Feng, G. Lei, Y.-q. He, R.-c. Wang, X.-f. Wang, Discharge performance of Mg-Al-Pb-La anode for Mg-air battery, Transactions of Nonferrous Metals Society of China, 28 (2018) 2274-2286.
[21] L. Fan, H. Lu, J. Leng, Z. Sun, Performance of Al-0.6 Mg-0.05 Ga-0.1 Sn- 0.1 In as Anode for Al-Air Battery in KOH Electrolytes, J Electrochem Soc, 162 (2015) A2623-A2627.
[22] P.H. J. Ma, X. Jia, C. Zhanga, G. Wang, Organic/inorganic double solutions for magnesium - air batteries, RSC Advances, 11 (2021) 7502-7510.
[23] D. Hoche, S.V. Lamaka, B. Vaghefinazari, T. Braun, R.P. Petrauskas, M. Fichtner, M.L. Zheludkevich, Performance boost for primary magnesium cells using iron complexing agents as electrolyte additives,

Scientific reports, 8 (2018) 7578.
[24] L. Wang, D. Snihirova, M. Deng, B. Vaghefinazari, S.V. Lamaka, D. Höche, M.L. Zheludkevich, Tailoring electrolyte additives for controlled Mg-Ca anode activity in aqueous Mg-air batteries, J Power Sources, 460 (2020) 228106.
[25] T.X. Zheng, Y.B. Hu, Y.X. Zhang, S.W. Yang, F.S. Pan, Composition optimization and electrochemical properties of Mg-Al-Sn-Mn alloy anode for Mg-air batteries, Mater Design, 137 (2018) 245-255.
[26] X. Chen, H. Wang, Q. Zou, Q. Le, C. Wen, A. Atrens, The influence of heat treatment on discharge and electrochemical properties of Mg-Gd-Zn magnesium anode with long period stacking ordered structure for Mg-air battery, Electrochimica Acta, 367 (2021) 137518.
[27] J. Li, B. Zhang, Q. Wei, N. Wang, B. Hou, Electrochemical behavior of Mg-Al-Zn-In alloy as anode materials in 3.5 wt.% NaCl solution, Electrochimica Acta, 238 (2017) 156-167.
[28] M. Curioni, The behaviour of magnesium during free corrosion and potentiodynamic polarization investigated by real-time hydrogen measurement and optical imaging, Electrochimica Acta, 120 (2014) 284-292.
[29] G. Williams, N. Birbilis, H.N. McMurray, The source of hydrogen evolved from a magnesium anode, Electrochemistry Communications, 36 (2013) 1-5.
[30] K.A. Yasakau, A. Maltseva, S.V. Lamaka, D. Mei, H. Orvi, P. Volovitch, M.G.S. Ferreira, M.L. Zheludkevich, The effect of carboxylate compounds on Volta potential and corrosion inhibition of Mg containing different levels of iron, Corros Sci, 194 (2022) 109937.
[31] R.M.S. Arthur E. Martell, Critical Stability Constants, Springer, Second supplement (1989).
[32] S.V. Lamaka, B. Vaghefinazari, D. Mei, R.P. Petrauskas, D. Hoche, M.L. Zheludkevich, Comprehensive screening of Mg corrosion inhibitors, Corros Sci, 128 (2017) 224-240.
[33] A. Maltseva, S.V. Lamaka, K.A. Yasakau, D. Mei, D. Kurchavov, M.L. Zheludkevich, G. Lefèvre, P. Volovitch, In situ surface film evolution during Mg aqueous corrosion in presence of selected carboxylates, Corros Sci, 171 (2020) 108484.
[34] J. Yang, C. Blawert, S.V. Lamaka, K.A. Yasakau, L. Wang, D. Laipple, M. Schieda, S. Di, M.L. Zheludkevich, Corrosion inhibition of pure Mg containing a high level of iron impurity in pH neutral NaCl solution, Corros Sci, 142 (2018) 222-237.
[35] S.V. Lamaka, D. Höche, R.P. Petrauskas, C. Blawert, M.L. Zheludkevich, A new concept for corrosion inhibition of magnesium: Suppression of iron re-deposition, Electrochemistry Communications, 62 (2016) 5-8.
[36] G.S. Frankel, A. Samaniego, N. Birbilis, Evolution of hydrogen at dissolving magnesium surfaces, Corros Sci, 70 (2013) 104-111.
[37] V. Moutarlier, M.P. Gigandet, B. Normand, J. Pagetti, EIS characterisation of anodic films formed on 2024 aluminium alloy, in sulphuric acid containing molybdate or permanganate species, Corros Sci, 47 (2005) 937-951.
[38] N. Wang, W. Li, Y. Huang, G. Wu, M. Hu, G. Li, Z. Shi, Wrought Mg-Al-Pb-RE alloy strips as the anodes for Mg-air batteries, J Power Sources, 436 (2019) 226855.
[39] X. Chen, W. Tian, S. Li, M. Yu, J. Liu, Effect of temperature on corrosion behavior of 3003 aluminum alloy in ethylene glycol–water solution, Chinese Journal of Aeronautics, 29 (2016) 1142-1150.
[40] M. Anik, I.M. Guneşdoğdu, Corrosion characteristics of Alloy AZ63 in buffered neutral solutions, Mater Design, 31 (2010) 3100-3105.
[41] F. Zucchi, V. Grassi, A. Frignani, C. Monticelli, G. Trabanelli, Electrochemical behaviour of a magnesium alloy containing rare earth elements, Journal of Applied Electrochemistry, 36 (2005) 195-

204.
[42] T.N. Vu, D. Veys-Renaux, E. Rocca, Potential bioactivity of coatings formed on AZ91D magnesium alloy by plasma electrolytic anodizing, Journal of biomedical materials research. Part B, Applied biomaterials, 100 (2012) 1846-1853.
[43] X. Liu, S. Liu, J. Xue, Discharge performance of the magnesium anodes with different phase constitutions for Mg-air batteries, J Power Sources, 396 (2018) 667-674.
[44] Y. Zhou, B. Wu, G. Lin, Z. Xing, S. Li, L. Deng, D. Chen, D. Yun, S. Xie, Interfacing Pristine C60 onto TiO2 for Viable Flexibility in Perovskite Solar Cells by a Low-Temperature All-Solution Process onto TiO2 for Viable Flexibility in Perovskite Solar Cells by a Low-Temperature All-Solution Process, Advanced Energy Materials, 8 (2018) 1800399.
[45] G.-L. Song, Z. Shi, Corrosion mechanism and evaluation of anodized magnesium alloys, Corros Sci, 85 (2014) 126-140.
[46] J. Li, Q. Jiang, H. Sun, Y. Li, Effect of heat treatment on corrosion behavior of AZ63 magnesium alloy in 3.5 wt.% sodium chloride solution, Corros Sci, 111 (2016) 288-301.
[47] Y.Q. Zhou, B.S. Wu, G.H. Lin, Y. Li, D.C. Chen, P. Zhang, M.Y. Yu, B.B. Zhang, D.Q. Yun, Enhancing Performance and Uniformity of Perovskite Solar Cells via a Solution-Processed C70 Interlayer for Interface Engineering, ACS applied materials & interfaces, 9 (2017) 33810-33818.
[48] A.D. King, N. Birbilis, J.R. Scully, Accurate Electrochemical Measurement of Magnesium Corrosion Rates; a Combined Impedance, Mass-Loss and Hydrogen Collection Study, Electrochimica Acta, 121 (2014) 394-406.
[49] M. Curioni, F. Scenini, T. Monetta, F. Bellucci, Correlation between electrochemical impedance measurements and corrosion rate of magnesium investigated by real-time hydrogen measurement and optical imaging, Electrochimica Acta, 166 (2015) 372-384.
[50] D.S. Guangling Song, The effect of zirconium grain refinement on the corrosion behaviour of magnesium-rare earth alloy MEZ, Journal of Light Metals, 2 (2002).
[51] D.K. Chanda, A. Samanta, A. Dey, P.S. Das, A.K. Mukhopadhyay, Nanoflower, nanoplatelet and nanocapsule Mg(OH)2 powders for adsorption of CO2 gas, Journal of Materials Science, 52 (2017) 4910-4922.
[52] T.B.R. D. Linden, Handbook of Batteries, McGraw-Hill, New York, Handbook of Batteries (2002).
[53] J.O.B. C. Daniel, Handbook of Battery Materials, John Wiley & Sons, Handbook of Battery Materials (2012).
[54] M. Deng, D. Hoche, S.V. Lamaka, D. Snihirova, M.L. Zheludkevich, Mg-Ca binary alloys as anodes for primary Mg-air batteries, J Power Sources, 396 (2018) 109-118.
[55] X. Liu, J. Xue, P. Zhang, Z. Wang, Effects of the combinative Ca, Sm and La additions on the electrochemical behaviors and discharge performance of the as-extruded AZ91 anodes for Mg-air batteries, J Power Sources, 414 (2019) 174-182.
[56] G.-L. Song, Z. Xu, Crystal orientation and electrochemical corrosion of polycrystalline Mg, Corros Sci, 63 (2012) 100-112.
[57] L.G. Bland, K. Gusieva, J.R. Scully, Effect of Crystallographic Orientation on the Corrosion of Magnesium: Comparison of Film Forming and Bare Crystal Facets using Electrochemical Impedance and Raman Spectroscopy, Electrochimica Acta, 227 (2017) 136-151.
[58] D. Mercier, J. Światowska, E. Protopopoff, S. Zanna, A. Seyeux, P. Marcus, Inhibition of Mg Corrosion by Sulfur Blocking of the Hydrogen Evolution Reaction on Iron Impurities, J Electrochem Soc, 167 (2020) 121504.

[59] A. Seyeux, M. Liu, P. Schmutz, G. Song, A. Atrens, P. Marcus, ToF-SIMS depth profile of the surface film on pure magnesium formed by immersion in pure water and the identification of magnesium hydride, Corros Sci, 51 (2009) 1883-1886.
[60] Y.Z. Y. Q. Zhou, J. T. Li, S. Zanna, A. Seyeux, P. Marcus, J. Światowska Organic/inorganic hybrid electrolyte for enhancing performance of Mg-air batteries Applied surface science, (Submitted) (2022).
[61] J.A. Yuwono, C.D. Taylor, G.S. Frankel, N. Birbilis, S. Fajardo, Understanding the enhanced rates of hydrogen evolution on dissolving magnesium, Electrochemistry Communications, 104 (2019) 106482.
[62] M. Santamaria, F. Di Quarto, S. Zanna, P. Marcus, Initial surface film on magnesium metal: A characterization by X-ray photoelectron spectroscopy (XPS) and photocurrent spectroscopy (PCS), Electrochimica Acta, 53 (2007) 1314-1324.
[63] M. Santamaria, F. Di Quarto, S. Zanna, P. Marcus, The influence of surface treatment on the anodizing of magnesium in alkaline solution, Electrochimica Acta, 56 (2011) 10533-10542.
[64] V. Fournier, P. Marcus, I. Olefjord, Oxidation of magnesium, Surface and Interface Analysis, 34 (2002) 494-497.
[65] Y. Wang, B. Liu, X. Zhao, X. Zhang, Y. Miao, N. Yang, B. Yang, L. Zhang, W. Kuang, J. Li, E. Ma, Z. Shan, Turning a native or corroded Mg alloy surface into an anti-corrosion coating in excited CO2, Nature communications, 9 (2018) 4058.
[66] D. Xue, Y. Yun, M.J. Schulz, V. Shanov, Corrosion protection of biodegradable magnesium implants using anodization, Materials Science and Engineering: C, 31 (2011) 215-223.
[67] B. Flamme, J. Światowska, M. Haddad, P. Phansavath, V. Ratovelomanana-Vidal, A. Chagnes, Sulfone Based-Electrolytes for Lithium-Ion Batteries: Cycling Performances and Passivation Layer Quality of Graphite and LiNi1/3Mn1/3Co1/3O2 Electrodes, J Electrochem Soc, 167 (2020) 070508.
[68] S.H. Salleh, S. Thomas, J.A. Yuwono, K. Venkatesan, N. Birbilis, Enhanced hydrogen evolution on Mg (OH)2 covered Mg surfaces, Electrochimica Acta, 161 (2015) 144-152.